NANO EXPRESS

Breaking the Symmetry of a Metal–Insulator–Metal-Based Resonator for Sensing Applications

Chung-Ting Chou Chao[1], Yuan-Fong Chou Chau[2*] and Hai-Pang Chiang[1*]

Abstract

This article designed a novel multi-mode plasmonic sensor based on a metal–insulator–metal waveguide side-coupled to a circular-shaped resonator containing an air path in the resonator. The electromagnet field distributions and transmittance spectra are investigated using finite element method-based simulations. Simulation results show that an air path in the resonator's core would impact the transmittance spectrum of SPPs. Besides, the air path is crucial in offering efficient coupling and generating multiple plasmon modes in the sensor system. The proposed structure has the advantage of multi-channel, and its sensitivity, figure of merit, and dipping strength can reach 2800 nm/RIU, 333.3 1/RIU, and 86.97%, respectively. The achieved plasmonic sensor can also apply for lab-on-chip in biochemical analysis for detecting the existence or nonappearance of diabetes through the human glucose concentration in urine.

Keywords: Biosensor, Circular-shaped resonator, Metal–insulator–metal waveguide, Finite element method

Introduction

Surface plasmon polaritons (SPPs) are the surface resonant excitations, including electromagnetic (EM) wave and collective electronic motions simultaneously, that the excitation happens at the interface of metal–dielectric boundary [1–9]. SPP waves have broad-ranging applications in optical devices and integrated optical circuits (IOCs) due to their advantage of overcoming diffraction limits and confining the light within the subwavelength regime [10–15]. As a result, different configurations of optical devices depending on SPP waveguides have been investigated and designed, such as absorbers [16, 17], filters [18, 19], amplifiers [20, 21], switches [22, 23], sensors [24–28]. Among them, SPP-based metal–insulator–metal (MIM) waveguides with strong light trapping, low ohmic loss, cost-effective fabrication, and long traveling path have attracted many research groups' consideration [29,

30]. MIM-cavity waveguide-based structure can design the plasmonic refractive index (RI) sensor due to the ease of compatibility with IOCs, compact size, and susceptible feature to a small change of ambient medium [31, 32].

Near-Infrared (NIR) spectroscopy is a potential analytical method that can get information on most chemical specimens with the merit of low power energy, less influence by heat and fluorescence, and nondestructive and label-free [33, 34]. However, the drawback of mismatching between sample sizes and NIR wavelength leads to limit sensitivity and spatial resolution [35]. MIM-cavity waveguide can solve this mismatch because the light fields can restrict and enhance in the nanoscale resonator [36]. However, the research field in NIR is rarely discussed based on MIM-cavity waveguides before, and this topic requires further investigation.

Resonance cavities with diverse shapes undergo a pivotal role in offering a preferable light-matter interaction in the MIM-cavity waveguide system [37, 38]. Recently, many research groups proposed various MIM-cavity schemes for constructing the plasmonic sensors, e.g., rectangular-shaped [39, 40], circular-shaped [41–43],

*Correspondence: chou.fong@ubd.edu.bn; hpchiang@mail.ntou.edu.tw
[1] Department of Optoelectronics and Materials Technology, National Taiwan Ocean University, Keelung 20224, Taiwan
[2] Centre for Advanced Material and Energy Sciences, Universiti Brunei Darussalam, Tungku Link, Gadong, Negara BE1410, Brunei Darussalam

Chou Chao *et al. Nanoscale Research Letters* (2022) 17:48

Page 2 of 14

elliptical-shaped [44, 45], crossed ring-shaped [46, 47], T-shaped [48, 49] cavities, and many other frameworks. The circular-shaped cavity is the most popular one due to the smooth surface, ease of fabrication, and small filling factor in a unit area [50, 51]. This paper reports a multimode plasmonic sensor based on a MIM bus waveguide side coupled to a circular-shaped resonator, including a rotational air path in the inner core working in the NIR wavelength range. We investigated and compared three configurations of side-coupled resonators, i.e., case 1 (one circular-shaped cavity), case 2 (one circular-shaped ring resonator), and case 3 (case 2 with an air path in the resonator's inner core), respectively. The finite element method (FEM) has been employed to analyze transmittance resonance modes and EM field distributions. In the case 3 structure, we use a rotational air path set in the resonator's core instead of a circular one to break the resonator's symmetry, which would impact the transmittance spectrum of SPPs. Modifying the geometry in the resonator's core can ameliorate the sensing performance. It is found that the air path can play a crucial role in providing efficient coupling between the bus waveguide and the resonator, breaking the structural symmetry, and offering an additional optical way in the proposed plasmonic system. Unlike the previously reported works, e.g., a horizontal air path and a vertical air stub [52] set in the resonator's inner core, the proposed case 3 structure possesses the merit of rotational air path, which can offer an additional degree of freedom (i.e., the rotational angle of the air path, θ) to facilitate the coupling effect between the bus waveguide and resonator. In addition, the proposed plasmonic sensor can also be applied for testing glucose concentration in human urine because it is easily accessible and is no bleeding. In practical situations, patients with diabetes must bleed blood for glucose testing, enduring pain, and causing uncomfortable. The novelty of this work is that we have measured the glucose concentration level in the urine specimens to detect diabetes in patients with 0.001 RI variation. To the best of our knowledge, we studied this issue using the SPPs MIM-cavity-based plasmonic sensor for the first time.

Methods and Fundamental

Figure 1a–c illustrates the top view of three sensor cases, i.e., case 1: a MIM bus waveguide (width w) side-coupled to a circular air cavity (radius $R+w$), case 2: case 1 with an inner core (radius R), and case 3: case 2 with an air path (width d) in the inner core, respectively. We indicated the structural parameters in Fig. 1a–c. They are the gap distance between the bus waveguide and the circular-shaped cavity (g), the displacement of the air path along the y-axis (s), and the angle of the air path (θ, an angle between the x-axis and

the center of air path), respectively. Note that s shifts the centers of the air path along the +y- axis or −y-axis. In Fig. 1, the gray- and white-colored regions represent the silver (Ag) and air. A TM-polarized EM wave coupled with the fundamental SPP mode [53–56] into the bus waveguide's input port, and the transmission power can reach the output port. The Drude model can describe Ag's frequency-dependent permittivity (ε_m) [57, 58].

$$\varepsilon_m(\omega) = \varepsilon_\infty - \frac{\omega_p^2}{\omega^2 + i\omega\gamma} \tag{1}$$

where $\varepsilon_\infty = 3.7$ is the infinite dielectric constant, ω stands for the frequency, $\omega_p = 9.10$ eV is bulk plasma frequency, and $\gamma = 18$ meV is the electron collision frequency, respectively.
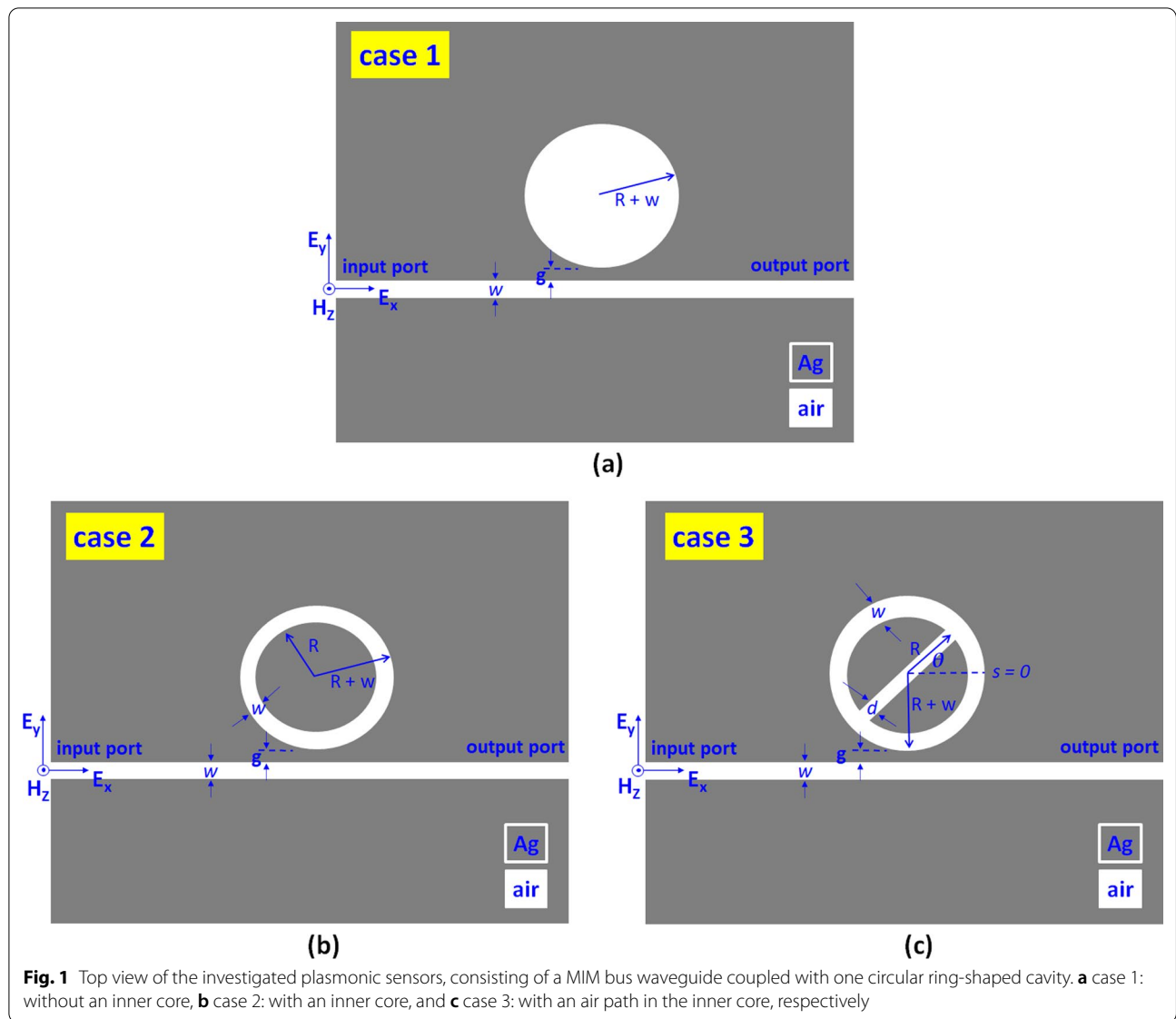
A 2D physical model replaces the 3D physical model because the structure height in the z-axis is much larger than the skin depth of SPPs in the x- and y- axes. COMSOL Multiphysics with the mesh size of ultrafine mesh grid size with the number of degrees of freedom of 68,815 to maintain the convergence of the results. Perfectly matched layers use to absorb the outgoing waves without reflection around the outer boundaries of the simulation domain. When the EM field impinges into the input port, it will reflect and transmit some energy, and part of it will couple into the ring resonator. The amount of reflected, transmitted, and coupled energy depend on the degree of coherent coupling and interference between the bus waveguide and the resonator. The circular-shaped ring resonator can serve as a Fabry–Pérot cavity, and the resonance will occur when the SPPs are side-coupled into the ring resonator and satisfy the resonance condition in the resonator. We can call the transmission modes as original modes of the ring resonator [59]. The SPPs can be excited when the incident EM wave approaches the intrinsic resonance wavelength (λ_{res}). If $\Delta\phi = 2\pi m$ (m is an integer), the λ_{res} can be expressed by temporal coupled-mode theory [60, 61].

$$\lambda_{res} = \frac{2L_{eff}\mathrm{Re}(n_{eff})}{m - \frac{\varphi}{2\pi}}(m = 1, 2, 3 \ldots) \tag{2}$$

Here m denotes the order of the standing wave resonance, L_{eff} represents the effective length of the resonator, ϕ stands for the phase shift, and $\mathrm{Re}(n_{eff})$ is the real part of the effective RI. n_{eff} can describe as:

$$\mathrm{Re}(n_{eff}) = \left(\varepsilon_{silver} + \left(\frac{k}{k_0}\right)^2\right)^{1/2} \tag{3}$$

where $k = 2\pi/\lambda$ is the wave vector, k_0 is the wave vector in the free space, and ε_{silver} is the silver's permittivity.

Chou Chao *et al. Nanoscale Research Letters*   (2022) 17:48

Page 3 of 14

Fig. 1 Top view of the investigated plasmonic sensors, consisting of a MIM bus waveguide coupled with one circular ring-shaped cavity. **a** case 1: without an inner core, **b** case 2: with an inner core, and **c** case 3: with an air path in the inner core, respectively

The input/output ports are located at the left/right ends of the designed device (see Fig. 1) to monitor the input/output powers. The transmittance (T) can obtain by $T = P_{out}$ (output power)/P_{in} (input power), where the P_{out} and P_{in} can calculate as integral values of energy flux density. The FWHM is full width at half-maximum, and the quality factor (QF) stands for the quality coefficient and can express as Eq. (4). The sensitivity (S) can calculate from Eq. (5). Besides, the figure of merit (FOM) can define by Eq. (6).

$$QF = \lambda_{res}/FWHM \tag{4}$$

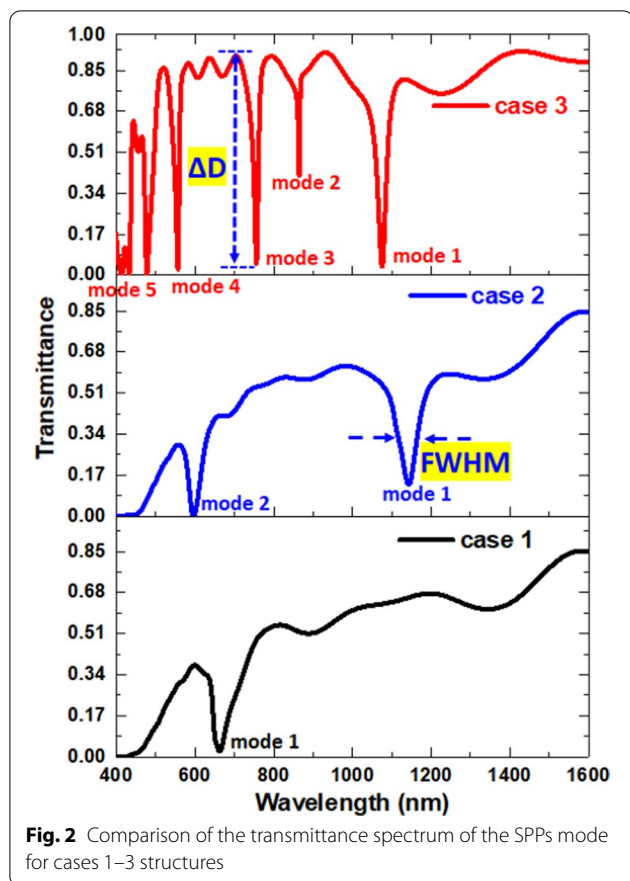$$S = \Delta\lambda_{res}/\Delta n (nm/RIU,\ nanometer\ per\ RI) \tag{5}$$

$$FOM = S/FWHM \tag{6}$$

where $\Delta\lambda_{res}$ is the shift of the λ_{res}, and Δn is the change of RI. Besides, we define the dipping strength (ΔD) in Eq. (7), i.e., the difference between the transmittance peak and dip [62]; see the inset of Fig. 2.

$$\Delta D = (T_{peak} - T_{dip}) \times 100\% \tag{7}$$

Results and Discussion

Figure 2 compares the transmittance spectrum for cases 1–3 structures. To guarantee that only the TM mode can travel in the investigated structure, we keep the bus waveguide width as $w = 50$ nm throughout this paper.

Fig. 2 Comparison of the transmittance spectrum of the SPPs mode for cases 1–3 structures

Table 1 Comparison of λ_{res}, FWHM, S, FOM, ΔD, and QF of cases 1–3 structures at resonance modes

	Mode 1	Mode 2	Mode 3	Mode 4	Mode 5
Case 1					
λ_{res} (nm)	663				
FWHM (nm)	45.00				
ΔD (%)	15.61				
S (nm/RIU)	600				
FOM (1/RIU)	13.33				
QF	14.73				
Case 2					
λ_{res} (nm)	1143	596			
FWHM (nm)	40.00	20.00			
S (nm/RIU)	1100	500			
FOM (1/RIU)	27.5	25.00			
ΔD (%)	32.68	29.52			
QF	28.58	29.80			
Case 3					
λ_{res} (nm)	1075	865	756	556	447
FWHM (nm)	20.00	3.00	10.00	10.00	10.00
S (nm/RIU)	1100	800	700	500	400
FOM (1/RIU)	55.00	266.67	70.00	50.00	40.00
ΔD (%)	80.90	53.11	85.81	85.30	86.18
QF	54.30	29.10	76.30	56.10	48.10

For testing the sensitivity, the RI value (*n*) is from 1.00 to 1.05 with an interval of 0.01

The default structural parameters, *R*, *g*, *s*, *θ*, and *d*, are 100 nm, 10 nm, 0 nm, 0°, and 50 nm, respectively. The resonator size of the proposed structure is compact and much smaller than many reported designs (e.g., [63, 64]). As seen, a distinct difference of the transmittance spectrum concerning the different resonance modes can elucidate this discrepancy after an air path appears in the proposed structure. The transmittance dips will redshift with the increase of the RI of filling dielectric [54]. The transmittance of the slit alone (i.e., only the bus waveguide in the plasmonic sensor system) exceeds 80% with the oscillating pattern in the wavelength range of 400–1600 nm [65], indicating that the incident light can transmit from the input port to the output port. As seen in Fig. 1, only one resonance mode occurred in case 1, which is associated with the original mode between the bus waveguide and resonator. In case 2, we found two transmittance dips corresponding to mode 1 and mode 2 in the wavelength range from 400 to 1600 nm, respectively. The two SPP modes attribute to the surface plasmon resonance (SPR) and cavity plasmon resonance (CPR) from the coupling effect between the bus waveguide and circular ring resonator [66–68]. When an air path exists in the resonator's core, case 3 can produce more SPP modes since the enhanced SPR and CPR, resulting in five SPP modes corresponding to mode 1 to mode 5, respectively. It will break the symmetry of the circular-shaped ring resonator with an air path instead of a split circular core, which could alter the propagation path of SPPs in the resonator. Note that the overall transmittance at off-resonance in case 3 is much higher than cases 1 and 2. This result can be attributed to the significant destructive interference (i.e., less light-matter interaction) between the bus waveguide and resonator at off-resonance, demonstrating the lower ohmic loss in the case 3 structure [69]. We compared the λ_{res}, FWHM, ΔD, S, FOM, and QF of cases 1–3 at corresponding resonance modes in Table 1. For testing the sensitivity, the RI value (*n*) is from 1.00 to 1.05 with an interval of 0.01. The interference of SPR and CPR causes the multiple SPP modes among bus waveguide and circular-shaped ring resonator. According to Fig. 2 and Table 1, we found that the air path acts as a critical role in offering a more significant number of plasmon modes, enhancing the coupling effect, breaking the structural symmetry, and creating an additional optical path. We can conclude that the resonance dip in case 3 has a more profound dip strength (ΔD), a narrower FWHM, and a higher QF than the other cases. These remarkable merits could help to improve the

RI-sensing performance. This noticeable characteristic of the case 3 structure gives way to the possible applications in nanophotonics devices.

To go into the physical nature, Fig. 3a, b illustrates the steady state of the magnetic field intensity (|H|) at the corresponding wavelengths of resonance modes and off-resonance modes in case 1 and case 2, respectively. As seen, the standing wave occurs in the circular-shaped ring resonator, and most input EM wave traps in the circular-shaped ring resonator at λ_{res}. The incident wavelength highly influences the |H| patterns of SPP modes due to the different phase and wave number

[44, 70]. The light spot number of |H| fields in circular-shape ring resonator are two for mode 1 in case 1, two, and four for modes 1–2 in case 2, and two, two, three, four, and five for modes 1–5 in case 3, respectively. The different spot number attributes to the variant phase significantly perturb the bus waveguide and circular-shaped ring resonator. For example, the shorter incident wavelength can experience more wavelengths in a fixed optical path, resulting in more light spot numbers. Therefore, we can find five light spots in mode 5 of the case 3 structure. The SPPs wave can confine in resonator well because of the constructive interference between the bus

Fig. 3 Truncate views of magnetic field intensity (|H|) at the corresponding wavelengths of resonance modes and off-resonance modes in **a** case 1, **b** case 2, and **c** case 3, respectively
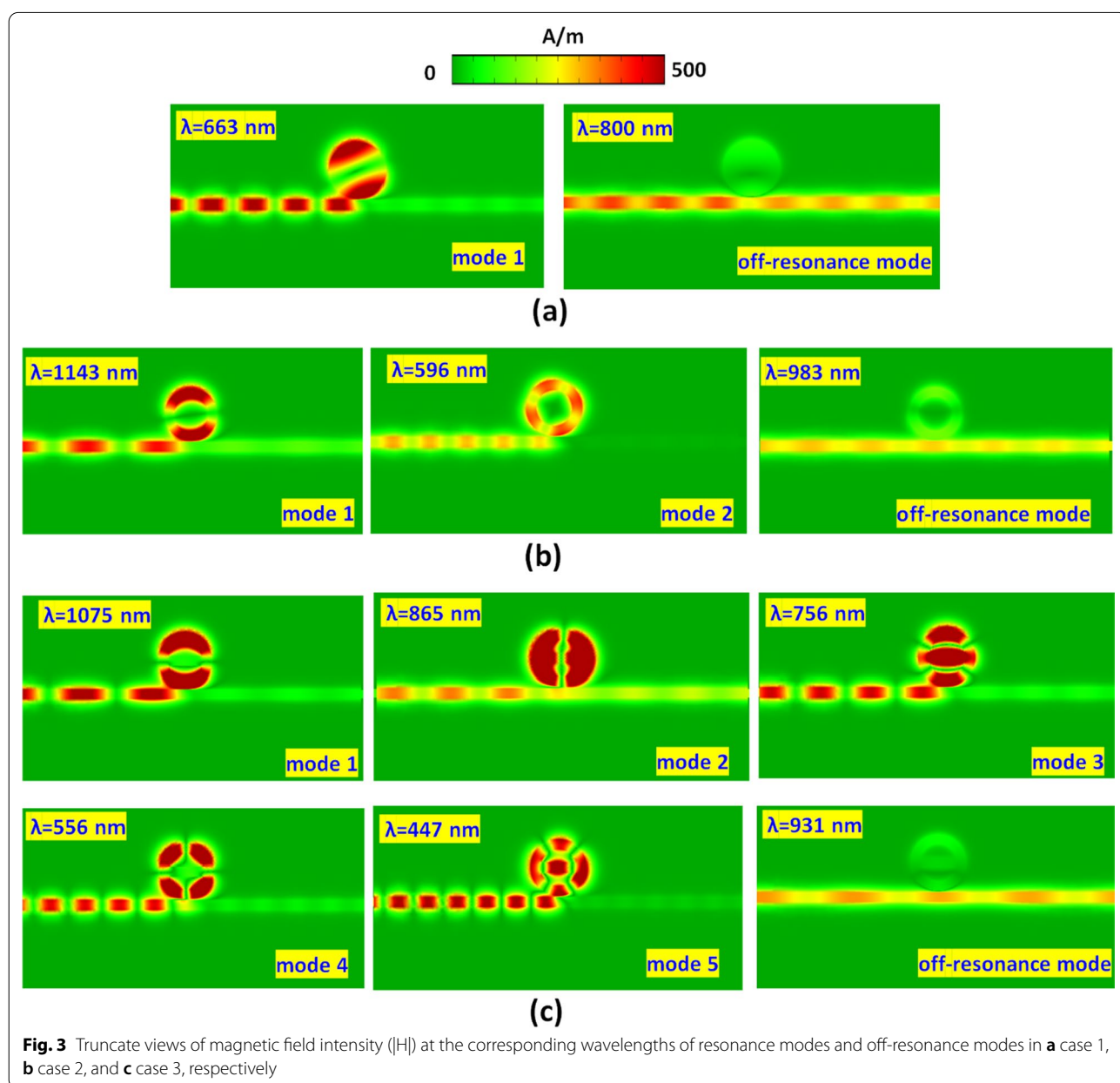
waveguide and the circular-shaped ring resonator, revealing remarkable CPR. The |H| field enhancement of the SPP modes exhibit an excellent light-matter coupling in the circular-shaped ring resonator. In Fig. 3a, b, the |H| fields are hardly trapped in the circular-shaped resonators at off-resonance mode due to the destructive interference between the bus waveguide and circular-shaped ring resonator, showing the higher transmittance values as observed in Fig. 2.

Next, we inspect the four structural parameters, i.e., *g*, *d*, *θ*, *s*, and *R*, that have a relatively significant influence on the optical properties of case 3 while keeping the other value of parameters intact. The default parameters of *w*, *g*, *d*, *θ*, *s*, and *R* are 50 nm, 10 nm, 50 nm, 0 nm, 0°, and 100 nm. First, we inspect the influence of the variation of *g* and *d* of the case 3 structure on the transmittance spectrum, as shown in Fig. 4a, b, respectively. As clearly observed in Fig. 4a, b, the transmittance dips of mode 1 blueshifts with the increasing *g* (from 1145 to 1048 nm) and *d* (from 1099 to 1009 nm), while the transmittance dips of other modes change slightly. The raising *g* diminishes the coupling effect between the bus

waveguides and the circular-shaped resonator. As seen, the transmittance profiles display a fierce oscillation due to a more significant coupling effect when *g*=0 nm. Furthermore, the ΔD and FWHM significantly reduce with the increase of *g* for mode 2 since a declining coupling effect as the extending value of *g*. Thus, the *d*'s value can alter the cavity's resonance condition and offer an optical path connected to both sides of the inner core. This feature hints that the balance of power flow strength of the discrete and the continuum state's SPPs mode is changed by varying *d*, the resonance conditions in the air path are affected. According to Fig. 4a, b, the available ranges of *g* and *d* based on the λ_{res}, transmittance curve shape, ΔD and FWHM are 5<*g*<25 nm and 30<*d*<90 nm, respectively, which reveals the reliability and robustness in the fabrication of proposed case 3 structure.

The coupling angle of EM wave between bus waveguide and the circular-shaped resonator can mediate the coupling effect and significantly influence the transmittance spectrum's profile. Figure 5a, b depicts the transmittance spectrum of varying *θ* and the selected magnetic field (|H|) intensities at the corresponding λ_{res} of the case 3
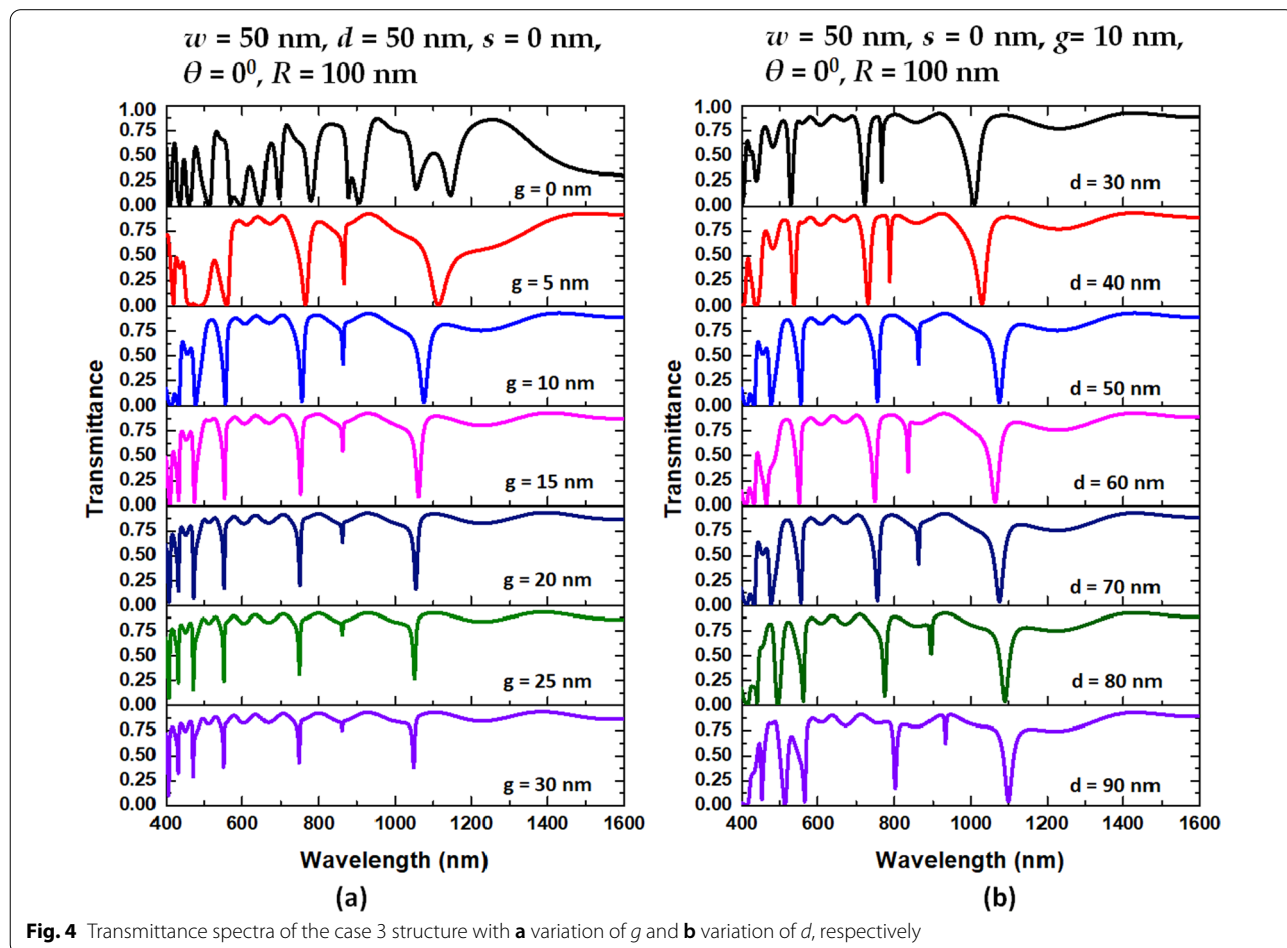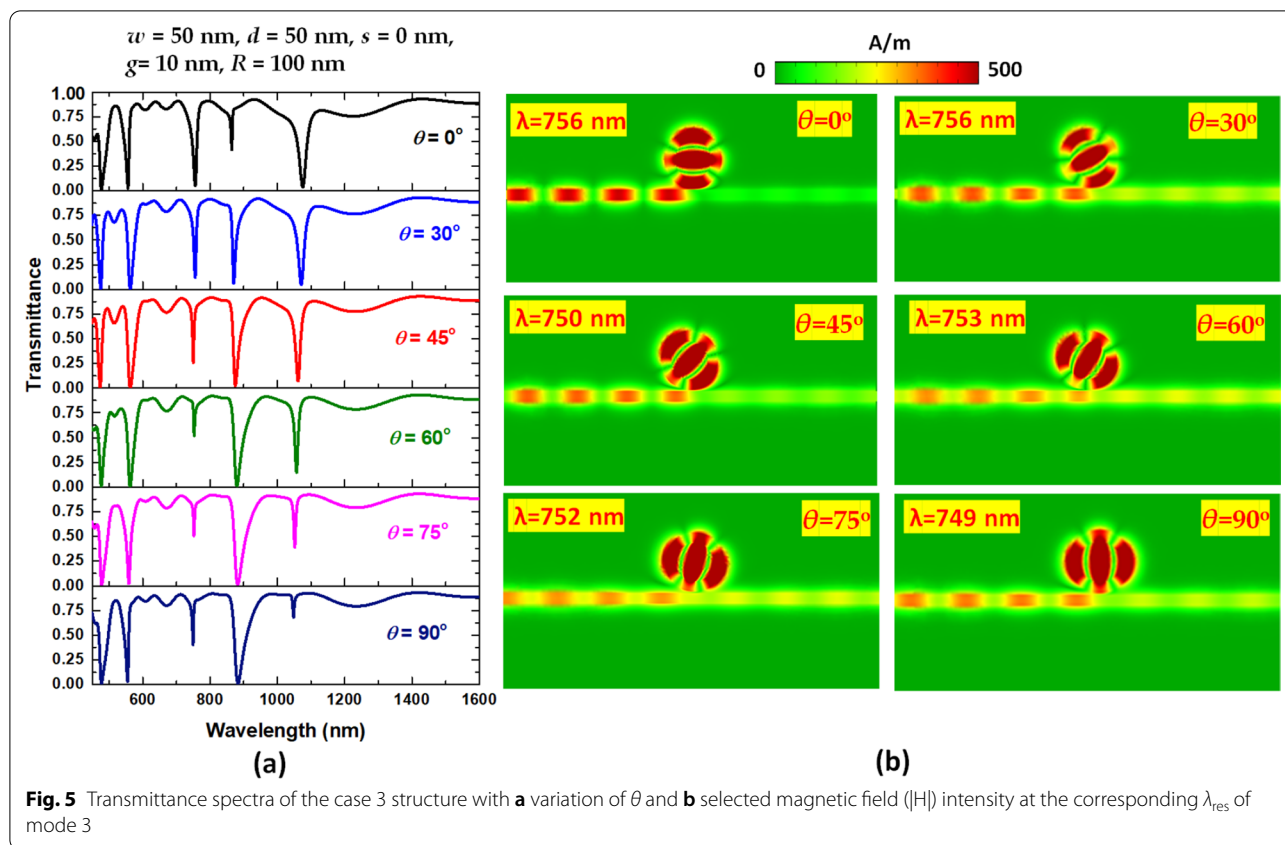

Fig. 4 Transmittance spectra of the case 3 structure with **a** variation of *g* and **b** variation of *d*, respectively

Fig. 5 Transmittance spectra of the case 3 structure with **a** variation of θ and **b** selected magnetic field (|H|) intensity at the corresponding λ_{res} of mode 3

structure. The transmittance spectra have different curve shapes to the variation of θ due to their different physical nature. We found five modes with variant ΔD in the 400–1600 nm wavelength range when θ varies from 0° to 90°. In Fig. 5a, the transmittance dips occur at λ_{res} when the air path has a rotational angle of θ. Compared with the symmetric structure ($\theta = 0°$), the sensing performance of the asymmetric case 3 structure is greatly improved when θ increases from 0° to 30°. For the asymmetric structure ($\theta > 0°$) because parts of EM wave locate at the magnetic nodes of the standing waves in the resonator, there is a transmittance dip [71]. As seen in Fig. 5a, the ΔD will rise with the increase of θ in modes 2 and 3, while the ΔD will reduce with the growth of θ in mode 1. The workable range of θ is 0° to 90°, and its optimal value is $\theta = 30°$ based on ΔD and the transmittance curve shape. Notably, the case of $\theta = 30°$ shows five dipper transmittance dips with ΔD in the range of 74.74–86.97% since this angle undergoes the preferential coupling angle between bus waveguide and circular-shaped ring resonator. It indicates that the proposed structure behaves as better light-matter coupling between the bus waveguide and resonator when $\theta = 30°$. The air path with a rotational angle of $\theta = 30°$ provides the strong confinement of SPPs and constructive interference in the circular-shaped

resonator. This finding attributes to the resonator's symmetry breaking, leading to the rotational air path's instinctive SPR and CPR modes. Compared to the case of $\theta = 90°$, only two transmittance dips can obtain due to the vertical coupling angle between the bus waveguide and resonator. We summarized the λ_{res}, FWHM, transmittance peaks ($T_{max.}$), transmittance dip ($T_{min.}$), ΔD and QF of case 3 structure at $\theta = 30°$ in Table 2. Modifying the geometry in the resonator's core can improve the sensing performance. One can conclude that the rotational angle of the air path in the resonator plays an essential

Table 2 Comparison of λ_{res}, FWHM, transmittance peaks ($T_{max.}$), and transmittance dip ($T_{min.}$), ΔD and QF of case 3 structure at $\theta = 30°$

	Mode 1	Mode 2	Mode 3	Mode 4	Mode 5
λ_{res} (nm)	1071	871	756	563	475
FWHM (nm)	20.00	10.00	8.00	12.00	10.00
T_{max}	91.87%	91.88%	90.74%	80.71%	75.59%
T_{min}	4.9%	6.5%	11.91%	0.80%	0.85%
ΔD (%)	86.97	85.38	78.83	79.91	74.74
QF	53.55	87.10	94.5	46.92	47.50

role in breaking the structure symmetry and dominating the coupling efficiency between the bus waveguide and circular-shaped resonator.

In Fig. 5b, the different incident wavelength influences the |H| field distributions at corresponding λ_{res} with different phases. The selected |H| fields at the corresponding λ_{res} of mode 3 in circular-shaped ring resonator show three petals of light spots, and the outline of air path match with the corresponding angle of θ. Besides, the dipolar effect could excite along both sides of the air path, i.e., resulting in positive–negative charge pairs. This phenomenon can dominate the field enhancement in the circular-shaped ring resonator. The air path in the inner circular-shaped core permits the highly trapped SPP modes and offers effective coupling efficiency and constructive interference in the resonator. Therefore, the apparent transmittance dips can observe in Fig. 5a.

Successively, we inspect the transmission spectra of case 3 structure by varying s and R, respectively. As shown in Fig. 6a, the suitable range of s is -40 to 40 nm. The number of resonance modes is two for $s = -40$ nm,

five for $s = -20$ and 0 nm, and six for $s = 20$ and 40 nm, indicating that a larger s with a larger distance between air path and bus waveguide will excite more resonance modes due to the enhanced CPR effect in the circular-shaped ring resonator. It is evident from Fig. 6b that the larger R can attain a greater mode number and offer flexibility in tuning transmittance's curve profile. Compared to other structural parameters, we found that the transmittance dip exhibits a remarkable redshift as the increase of R. This is because of the rise of effective length (L_{eff}) of the resonator, which is in good agreement with Eq. (2). We notice that the shift of λ_{res} by varying R is more sensitive than θ, s, d, and g. Hence, we can choose the specific transmittance dip to the characteristic wavelengths by varying R. The mode number is three, five, seven, seven, nine, and nine for $R = 50$, 100, 150, 200, 250, and 300 nm in the wavelength range of 450–3000 nm, accordingly. Table 3 displays the λ_{res}, S, and FOM of the case 3 structure when R is varied from 50 to 300 nm with an increment of 50 nm in the 450–3000 nm wavelength range, respectively. The RI of surrounding media,
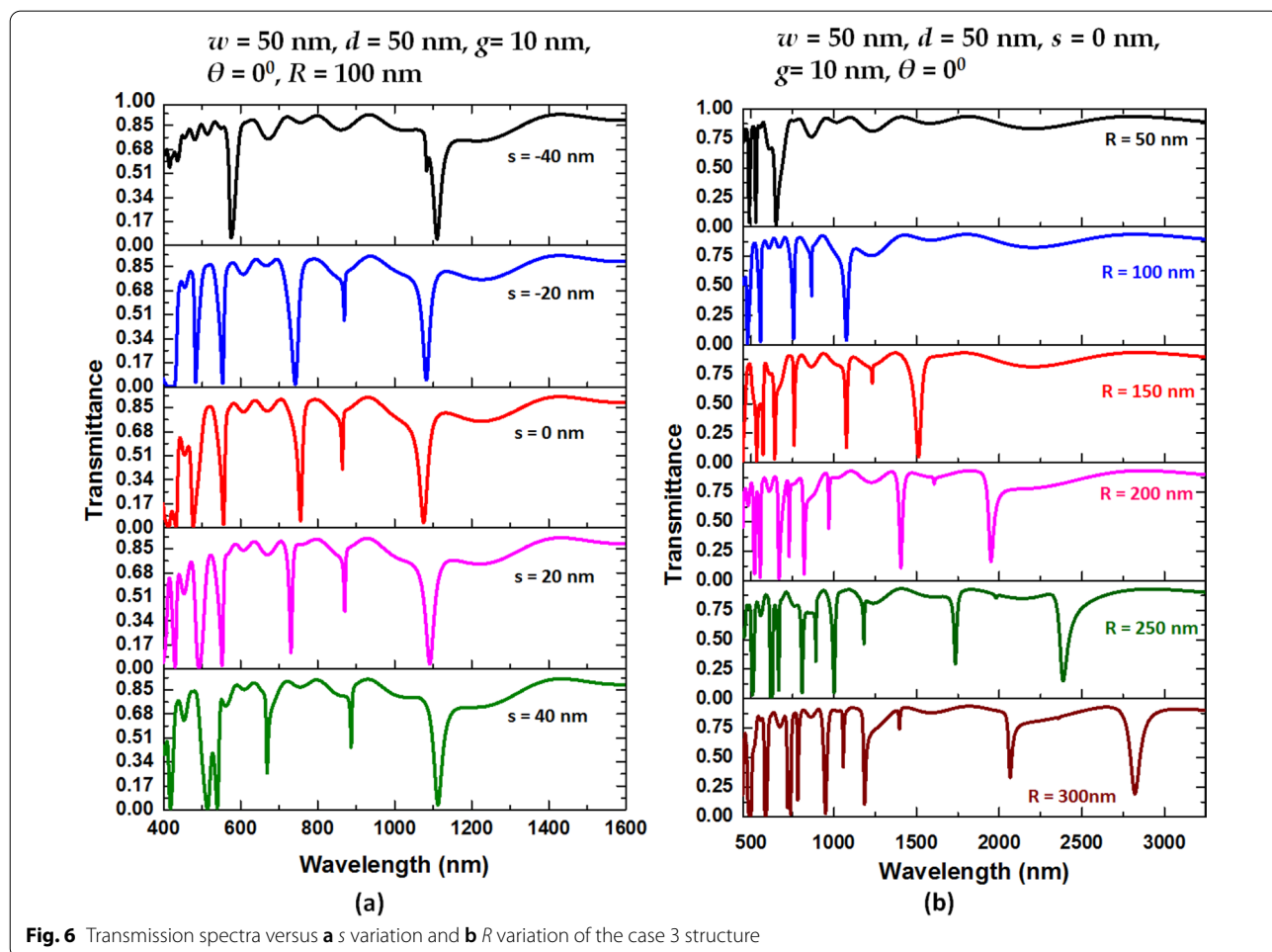

Fig. 6 Transmission spectra versus **a** *s* variation and **b** *R* variation of the case 3 structure

Table 3 The λ_{res}, S, and FOM corresponding to the resonance modes of the case 3 structure when R is varied from 50 to 300 nm with an increment of 50 nm in the wavelength range of 450–3000 nm, respectively
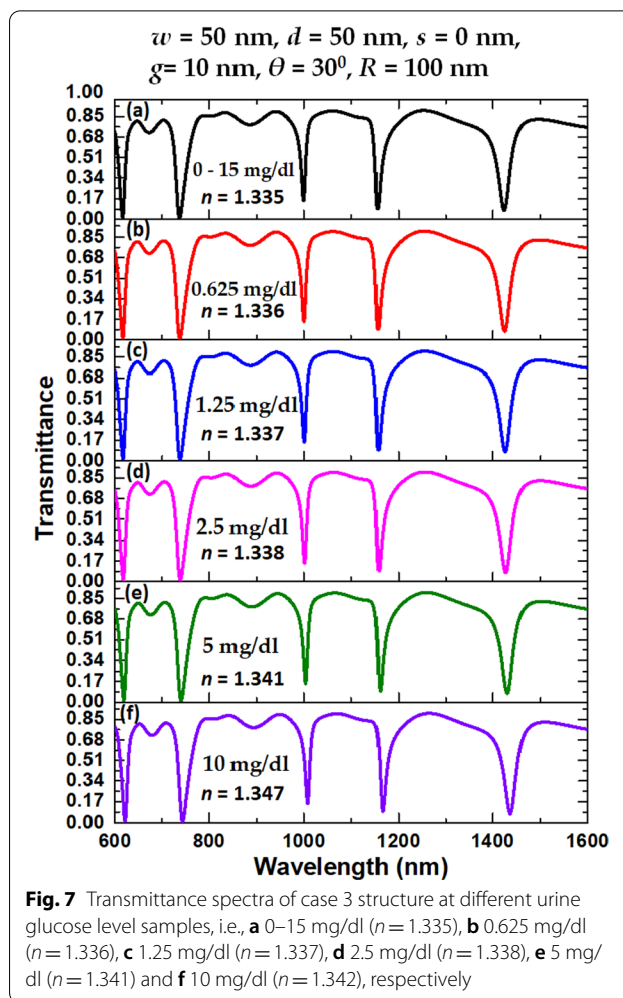
Mode		1	2	3	4	5	6	7	8	9
$R = 50$ nm	λ_{res} (nm)	661	528	487						
	S(nm/RIU)	400	400	400						
	FOM(1/RIU)	13.3	66.7	50.0						
$R = 100$ nm	λ_{res} (nm)	1075	865	756	556	447				
	S(nm/RIU)	1100	800	700	500	400				
	FOM(1/RIU)	55.0	266.7	70.0	50.0	40.0				
$R = 150$ nm	λ_{res} (nm)	1512	1232	1076	759	642	572	533		
	S(nm/RIU)	1500	1300	1100	700	600	600	500		
	FOM(1/RIU)	50.0	260.0	110.0	87.5	75.0	150.0	71.4		
$R = 200$ nm	λ_{res} (nm)	1951	1405	970	820	729	554	520		
	S(nm/RIU)	1900	1400	900	800	700	500	500		
	FOM(1/RIU)	63.3	56.0	225.0	100.0	62.5	62.5	71.4		
$R = 250$ nm	λ_{res} (nm)	2387	1735	1182	1001	891	808	666	617	507
	S(nm/RIU)	2400	1700	1200	1000	1000	700	700	600	400
	FOM(1/RIU)	48.0	113.3	240.0	83.3	333.3	175.0	233.3	40.0	40.0
$R = 300$ nm	λ_{res} (nm)	2822	2026	1397	1186	782	737	719	588	495
	S(nm/RIU)	2800	2100	1300	1100	800	700	700	500	500
	FOM(1/RIU)	30.0	105.0	216.7	110.0	160.0	140.0	140	33.3	25.0

n, is 1.00–1.04 with an interval of 0.01. The calculated S can reach 2800, 2100, 1300, 1100, 1100, and 800 nm/RIU, while the FOM can get 30.0, 105.0, 216.7, 110.0, and 160.0 for modes 1–5 when $R = 300$ nm. Besides, these values are superior to the published articles (e.g., [72, 73],). Based on Fig. 6b, the workable values of R are in the range of 50 nm $< R <$ 300 nm. It will confront to prepare the proposed sensor when R's value is too small (e.g., $R < 50$ nm), yet if R's value is too big (e.g., $R > 300$ nm), the device's size, ΔD, FWHM, and ohmic loss [74] will get large [75], which is then useless. Based on Fig. 6b, we can conclude that the size of R will significantly contribute to the sensitivity performance to the proposed case 3 structure and enhance the CPR effect in the coupled resonator. It should note that the resonance mode's intensity during RI sensing (dipping strength, i.e., $\Delta D = T_{peak} - T_{dip}$) directly influences the sensing accuracy as it is easier to inspect the sensing signal with a strong resonance [62]. The more ohmic losses raised by a longer optical path since the confinement loss is inevitable in the plasmonic MIM waveguide. It is evident in Fig. 6b that the dipping strengths exhibit a little difference (e.g., ΔD varies from 87.5% to 77.5% for mode 1) when R varies from 50 to 300 nm. The coupling EM wave could well confine in the resonator, showing a bonding resonance mode [76]. This finding demonstrates that the proposed case 3 structure possesses the advantage of low ohmic loss [77]. Thus, one can flexibly tune the desired working wavelength by varying the R's value in the range of 50 nm $< R <$ 300 nm.

Diabetes is a lasting metabolic disturbance disease arising from blood glucose (blood sugar) levels, which seriously harms the nervous system, kidneys, eyes, and heart [78]. One can demonstrate that human urine samples will change with the glucose concentration (GC) levels [79]. In typical situations, the human body has glucose ranging from 0 to 15 mg per deciliter (mg/dl) [80]. However, GC levels in human urine will rise to the average range of 165–180 mg/dl due to glycosuria. In Ref. [80], Sani et al. numerically investigated the change of GC level with RI using nanocavity of photonic crystal waveguide [81]. Moreover, Mostufa and coauthors analyzed the different urine GC level samples using graphene-coated SPR-based biosensor [79]. Here, we will examine the sensing performance using the MIM-cavity waveguide-based structure (i.e., case 3) for the first time to the best of our knowledge.

Near-infrared (NIR) ranging in 0.75 ~ 3.0 μm is a low power intensity light that the irradiation effects are a response to the light but not to the heat [33]. Thus, it is suitable to detect the presence or absence of diabetes through the human GC in urine with specific λ_{res} ranging in NIR. This section will detect the GC levels in human urine using the proposed case 3 structure. Before that, we should select a suitable range of operation wavelengths. Infrared spectroscopy is a potential analytical method that can obtain information on the chemical composition of most specimens. As shown in Fig. 5a, the wavelengths corresponding to the case 3 structure at $\theta = 30°$ have
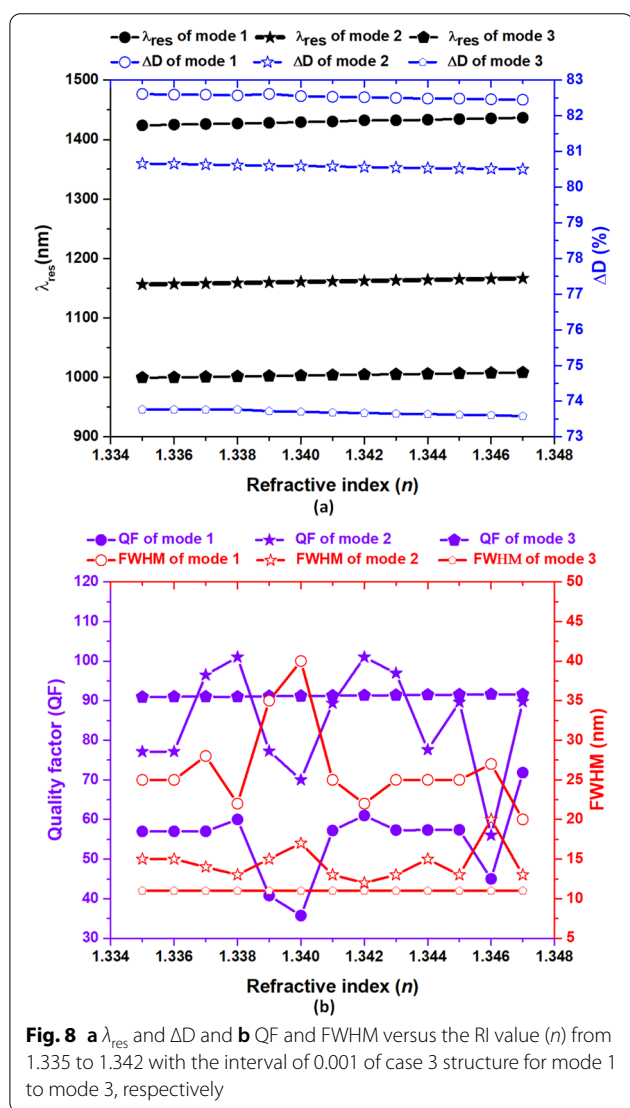
three distinct resonance modes (i.e., modes 1–3) in this range. Thus, we adopted case 3 as the candidate based on excellent sensing performance and compact size (see Table 2). The sensor function of the case 3 structure utilizes the resonance cavity filled with specimens, and the same method can be applied to all cases of RI sensing. Depending on the RI of the human GC, each sample offers a specific resonance wavelength. As described in Ref. [82], diabetes has a very high RI. Filling the human urine specimens inside the circular-shaped resonator of the case 3 structure will lead to a RI shift (Δn) due to a GC level increment in urine samples. The plasmonic sensor would detect that by shifting the λ_{res}, one can determine the main resonance modes in the case 3 structure by the circular-shaped resonator of a specific resonant wavelength concerning the GC in the human urine. Figure 7a–f depicts the transmittance spectrum of case 3 structure at different urine glucose level samples, i.e., 0–15 mg/dl ($n = 1.335$), 0.625 mg/dl ($n = 1.336$), 1.25 mg/dl ($n = 1.337$), 2.5 mg/dl ($n = 1.338$), 5 mg/dl ($n = 1.341$), and 10 mg/dl ($n = 1.342$), respectively. As seen, each case has five transmittance dips, and it can separate the shift of resonance wavelength (λ_{res}), resulting in the normal person partitioning into the patient. The recently introduced detectors have a solution of detecting a wavelength shift as small as 0.1 nm. For the variation of GC in (0–15, 0.625) mg/dl (Fig. 7a, b), the corresponding λ_{res} shift from 1423.9–1425.0 nm for mode 1, 1156.3–1157.2 nm for mode 2, and 999.4–1000.1 nm for mode 3, to the Δn of 0.001. The recorded (S, FOM) reach (1100 nm/RIU, 36.67 RIU^{-1}), (900 nm/RIU, 180.00 RIU^{-1}), and (700 nm/RIU, 70.00 RIU^{-1}) corresponding to mode 1 to mode 3, accordingly. In the same manner, for two levels of GC in (1.25, 2.5) mg/dl in human urine (Fig. 7c, d), the corresponding λ_{res} change from 1426.0–1427.1 nm for mode 1, 1158.0–1158.9 nm for mode 2, and 1000.8–1001.6 nm for mode 3, to the Δn of 0.001. The (S, FOM) achieve (1100 nm/RIU, 36.67 RIU^{-1}), (900 nm/RIU, 180.00 RIU^{-1}), and (800 nm/RIU, 80.00 RIU^{-1}) corresponding to mode 1 to mode 3, accordingly. Similarly, for the case of GC in (5, 10) mg/dl in human urine (Fig. 7e, f), the corresponding λ_{res} vary from 1430.2–1436.7 nm for mode 1, 1161.4–1166.6 nm for mode 2 and 1003.8–1008.1 nm for mode 3, to the Δn of 0.006. The (S, FOM) reach (1183 nm/RIU, 36.10 RIU^{-1}), (866 nm/RIU, 173.20 RIU^{-1}), and (716 nm/RIU, 71.60 RIU^{-1}) corresponding to mode 1 to mode 3, accordingly. Therefore, we can detect the human urine samples by observing the λ_{res} shift in the transmittance spectrum using the proposed case 3 structure. Table 4 summarizes the λ_{res} (nm), S (nm/RIU), and FOM (1/RIU) of case 3 structure in different GC levels of patient urine samples corresponding to mode 1 to mode 3, respectively. Figure 8 also depicts λ_{res} and ΔD (Fig. 8a), and QF

Fig. 7 Transmittance spectra of case 3 structure at different urine glucose level samples, i.e., **a** 0–15 mg/dl ($n = 1.335$), **b** 0.625 mg/dl ($n = 1.336$), **c** 1.25 mg/dl ($n = 1.337$), **d** 2.5 mg/dl ($n = 1.338$), **e** 5 mg/dl ($n = 1.341$) and **f** 10 mg/dl ($n = 1.342$), respectively

and FWHM (Fig. 8b) versus the RI value from 1.335 to 1.342 with the interval of 0.001 of case 3 structure corresponding mode 1 to mode 3. Besides, the sensor's ΔD is associated with the transmittance intensity (%) difference, which is closely related to the detecting accuracy and resolution. In Fig. 8a, as the RI increases, the λ_{res} increases linearly, and the recorded values of ΔD are in the range of 82.45–82.61% for mode 1, 80.50–80.60% for mode 2, and 73.58–73.77% for mode 3, showing the excellent values in modes 1–3. In Fig. 8b, we calculate the effects of RI changes on QF and FWHM. As seen, if the RI = 1.338 and 1.342, the QF reaches its highest value, and the two lowest values are found at RI = 1.340 and 1.346 for mode 1 and mode 2, while QF values are around 90.00 for mode 3, respectively. Therefore, we can conclude that the sensor structure for detecting GC levels in urine samples of the diabetic patient with a RI of 1.338 and 1.342 is highest and is minimized at a RI of 1.340 and 1.346, respectively. Besides, the FWHM values are in the range of 20–40 nm for mode 1, 12–15 nm for mode 2, and around 5–10 nm

Chou Chao *et al. Nanoscale Research Letters*   (2022) 17:48

Page 11 of 14

Table 4 λ_{res} (nm), S (nm/RIU), and FOM (1/RIU) of case 3 structure in different GC of patient urine samples corresponding to mode 1 to mode 3

Glucose	RI	Δ*n*	Mode 1			Mode 2			Mode 3		
			λ_{res}	S	FOM	λ_{res}	S	FOM	λ_{res}	S	FOM
0–15 mg/dl	1.335	Ref	1423.9	Ref	Ref	1156.3	Ref	Ref	999.4	Ref	Ref
0.625 mg/dl	1.336	0.001	1425.0	1100	36.67	1157.2	900	180.0	1000.1	700	63.64
1.25 mg/dl	1.337	Ref	1426.0	Ref	Ref	1158	Ref	Ref	1000.8	Ref	Ref
2.5 mg/dl	1.338	0.001	1427.1	1100	36.67	1158.9	900	180.0	1001.6	800	72.73
5 mg/dl	1.341	Ref	1430.2	Ref	Ref	1161.4	Ref	Ref	1003.8	Ref	Ref
10 mg/dl	1.347	0.006	1436.7	1083	36.10	1166.6	866	173.2	1008.1	716	65.09

Fig. 8 a λ_{res} and ΔD and **b** QF and FWHM versus the RI value (*n*) from 1.335 to 1.342 with the interval of 0.001 of case 3 structure for mode 1 to mode 3, respectively

for mode 3; these values guarantee the accurate measurement of the GC level in urine samples due to the low FWHM with the best average bandwidth wavelength.

Besides, the proposed case 3 structure can also serve as a temperature sensor to detect the thermal medium. A change in the temperature leads to a variation in the RI of the sensing medium [83, 84]. As a temperature sensor, a liquid, e.g., ethanol, with high RI temperature coefficient (3.94×10^4) is filled into the resonator and bus waveguide region, which is then sealed [85, 86].

Comparison of the sensitivity and figure of merit between this work and selected published works is given in Table 5. Based on Table 5 and the simulation results mentioned above, the proposed case 3 structure's obtained sensitivity is remarkably higher than those of similar MIM designs reported in the literature.

Conclusion

This study proposed a plasmonic sensor based on a side-coupled circular-shaped ring resonator in a MIM-cavity waveguide system for RI and biomedical sensor applications. Three cases of resonators are investigated and compared, i.e., case 1 (one circular-shaped cavity), case 2 (one circular-shaped ring resonator), and case 3 (case 2 with an air path in the resonator's core), respectively. We analyzed transmittance resonance modes and EM field distributions in detail using FEM-based simulations. An air path set in the resonator's core instead of a circular core can break the resonator's symmetry, impacting the transmittance spectrum of SPPs. It is found that the rotational angle of the air path in the resonator's core plays a pivotal role in breaking the structure symmetry and dominating the coupling efficiency between bus waveguide and circular-shaped ring resonator. Modifying the resonator's core geometry can enhance the sensing performance and keep the structure size unchanged. When $R = 300$ nm, the sensitivity, figure of merit, and dipping strength can reach 2800 nm/RIU, 333.3 1/RIU, and 86.97%, respectively. The proposed case 3 with $R = 100$ nm can detect a different

Table 5 Comparison of the sensitivity and FOM between this work and previous similar works

Reference/year	Structure	Max. sensitivity (nm/RIU)	Max. FOM (1/RIU)
[87]/2017	Two circular cavities	840	100
[88]/2018	Side-coupled stub-hexagon resonators	550	178.00
[89]/2019	Rectangular ring resonator	1367	22.30
[26]/2020	Resonator with taped defects	1295	159.60
[90]/2021	Clockwork spring-shaped resonator	1210	191.16
This work	Resonator with a rotational air path	2800	333.30

glucose concentration level from a healthy person by human urine specimens for each 0.001 RI change. The sensitivity can simultaneously operate in multiple modes and reach above 700 nm/RIU in modes 1–3. The minimum FWHM is ~ 5.0 nm, and the maximum FOM is 80.0 1/RIU. Besides, the dipping strength shows the excellence values ranging in 74.74%–86.97% in modes 1–5, while the recorded Q factors are in the range of 46.92–87.10 in modes 1–5. The proposed sensor is a promising candidate for nanophotonics and biochemistry since its excellent sensing performance with multiple modes and broad operation wavelengths.

Abbreviations
SPPs: Surface plasmon polaritons; EM: Electromagnetic; IOCs: Integrated optical circuits; MIM: Metal–insulator–metal; RI: Refractive index; NIR: Near-infrared; FEM: Finite element method; FWHM: Full width at half-maximum; QF: Quality factor; S: Sensitivity; FOM: Figure of merit; ΔD: Dipping strength; SPR: Surface plasmon resonance; CPR: Cavity plasmon resonance; |H|: Magnetic field intensity; GC: Glucose concentration.

Author Contributions
C-TCC was involved in investigation, simulation, and data analysis, YFCC contributed to investigation, resources, conceptualization, and writing. H-PC did conceptualization, methodology, writing—review and editing. All authors read and approved the final manuscript.

Availability of Data and Materials
Not applicable.

Declarations

Competing interests
The authors report no declarations of interest.

References
1. Wang K, Chen L, Zhang H, Hsiao HH, Tsai DP, Chen J (2017) Plasmon-enhanced optical nonlinearity for femtosecond all-optical switching. Appl Phys Lett 111(18):181102
2. Chau Y-F, Jiang Z-H, Li H-Y, Lin G-M, Fong-Lin Wu, Lin W-H (2011) Localized resonance of composite core-shell nanospheres, nanobars and nano-spherical chains. Prog Electromagn Res B 28:183–199
3. Chen MW, Chau YF, Tsai DP (2008) Three-dimensional analysis of scattering field interactions and surface plasmon resonance in coupled silver nanospheres. Plasmonics 3(4):157–164
4. Chau Y-F (2009) Surface plasmon effects excited by the dielectric hole in a silver-shell nanospherical pair. Plasmonics 4(4):253
5. Ho YZ, Chen WT, Huang YW, Wu PC, Tseng ML, Wang YT, Tsai DP (2012) Tunable plasmonic resonance arising from broken-symmetric silver nanobeads with dielectric cores. J Opti 14(11):114010
6. Sung M-J, Ma Y-F, Chau Y-F, Huang D-W (2010) Surface plasmon resonance in a hexagonal nanostructure formed by seven core shell nanocylinders. Appl Opt 49(5):920–926
7. Peng TC, Lin WC, Chen CW, Tsai DP, Chiang HP (2011) Enhanced sensitivity of surface plasmon resonance phase-interrogation biosensor by using silver nanoparticles. Plasmonics 6(1):29–34
8. Chen WT, Wu PC, Chen CJ, Chung HY, Chau YF, Kuan CH, Tsai DP (2021) Electromagnetic energy vortex associated with sub-wavelength plasmonic Taiji marks. Opt Express 18(19):19665–19671
9. Chau YF, Yeh HH, Tsai DP (2007) Significantly enhanced birefringence of photonic crystal fiber using rotational binary unit cell in fiber cladding. Jpn J Appl Phys 46(11L):L1048
10. Shen L, Yang TJ, Chau YF (2007) 50/50 beam splitter using a one-dimensional metal photonic crystal with parabolalike dispersion. Appl Phys Letters 90(25):251909
11. Zhang J, Zhang L (2012) Nanostructures for surface plasmons. Adv Opt Photon 4(2):157–321
12. Singh L, Maccaferri N, Garoli D, Gorodetski Y (2021) Directional plasmonic excitation by helical nanotips. Nanomaterials 11(5):1333
13. Zhu J, Wang Ge, Jiang F, Qin Y, Cong Hu (2019) Temperature sensor of Mos2 based on hybrid plasmonic waveguides. Plasmonics 14(6):1863–1870
14. Hsieh LZ, Chau YF, Lim CM, Lin MH, Huang HJ, Lin CT, Syafi'ie MI (2016) Metal nano-particles sizing by thermal annealing for the enhancement of surface plasmon effects in thin-film solar cells application. Opt Commun 370:85–90
15. Shen L, Yang TJ, Chau YF (2008) Effect of internal period on the optical dispersion of indefinite-medium materials. Phys Rev B 77(20):205124
16. Wu P, Zhang C, Tang Y, Liu B, Lv Li (2020) A perfect absorber based on similar Fabry–Perot four-band in the visible range. Nanomaterials 10(3):488
17. Chou Chao CT, Chou Chau YF, Huang HJ, Kumara NT, Kooh MR, Lim CM, Chiang HP (2020) Highly sensitive and tunable plasmonic sensor based on a nanoring resonator with silver nanorods. Nanomaterials 10(7):1399
18. Neutens P, Lagae L, Borghs G, Van Dorpe P (2012) Plasmon filters and resonators in metal-insulator-metal waveguides. Opt Express 20(4):3408–3423
19. Lin J-M, Chau Y-F (1995) Radome slope compensation using multiple-model kalman filters. J Guid Control Dyn 18(3):637–640

20. Zhang T, Feng S (2014) Development and application of surface plasmon polaritons on optical amplification. J Nanomater 2014 2014:495381
21. Izadi MA, Nouroozi R (2018) Adjustable propagation length enhancement of the surface plasmon polariton wave via phase sensitive optical parametric amplification. Sci Rep 8(1):1–4
22. Sahu PP (2021) Optical switch based on graphene clad two surface plasmonic polariton mode coupler. Optik 227:166026
23. Bashiri S, Fasihi K (2020) An all-optical 1 × 2 demultiplexer using Kerr nonlinear nano-plasmonic switches. Plasmonics 15(2):449–456
24. Zhu J, Li Na (2020) MIM waveguide structure consisting of a semicircular resonant cavity coupled with a key-shaped resonant cavity. Opt Express 28(14):19978–19987
25. Chen Y, Luo P, Liu X, Di Y, Han S, Cui X, He L (2018) Sensing performance analysis on fano resonance of metallic double-baffle contained MDM waveguide coupled ring resonator. Opt Laser Technol 101:273–278
26. Rahmatiyar M, Afsahi M, Danaie M (2020) Design of a refractive index plasmonic sensor based on a ring resonator coupled to a MIM waveguide containing tapered defects. Plasmonics 15(6):2169–2176
27. Wen K, Yihua Hu, Chen Li, Zhou J, Lei L, Guo Z (2014) Fano resonance with ultra-high figure of merits based on plasmonic metal–insulator–metal waveguide. Plasmonics 10:27–32
28. Zhang ZD, Wang HY, Zhang ZY (2013) Fano resonance in a gear-shaped nanocavity of the metal–insulator–metal waveguide. Plasmonics 8(2):797–801
29. Li C, Qi D, Xin J, Hao F (2014) Metal–insulator–metal plasmonic waveguide for low-distortion slow light at telecom frequencies. J Mod Opt 61(8):627–630
30. Kwon M-S (2011) Metal–insulator–silicon–insulator–metal waveguides compatible with standard Cmos technology. Opt Express 19(9):8379–8393
31. Khonina SN, Kazanskiy NL, Butt MA, Kaźmierczak A, Piramidowicz R (2021) Plasmonic sensor based on metal-insulator-metal waveguide square ring cavity filled with functional material for the detection of Co2 gas. Opt Express 29(11):16584–16594
32. Al Mahmud R, Faruque M, Sagor RH (2021) Plasmonic refractive index sensor based on ring-type pentagonal resonator with high sensitivity. Plasmonics 16(3):873–880
33. Tsai SR, Hamblin MR (2017) Biological effects and medical applications of infrared radiation. J Photochem Photobiol B Biol 170:197–207
34. Bećb KB, Grabska J, Huck CW (2020) Near-infrared spectroscopy in bio-applications. Molecules (Basel, Switzerland) 25(12):2948
35. Chen L, Liu Y, Zhongyuan Yu, Dong Wu, Ma R, Zhang Y, Ye H (2016) Numerical analysis of a near-infrared plasmonic refractive index sensor with high figure of merit based on a fillet cavity. Opt Express 24(9):9975–9983
36. Zhou YJ, Xiao QX, Jia Yang B (2015) Spoof localized surface plasmons on ultrathin textured MIM ring resonator with enhanced resonances. Sci Rep 5(1):1–2
37. Chen Y, Liu Y, Chen Z, Jiao R, Li Yu (2016) Fano resonance in a symmetric waveguide system with different filled insulators. Opt Commun 371:184–188
38. Butt MA, Kazanskiy NL, Khonina SN (2020) Highly integrated plasmonic sensor design for the simultaneous detection of multiple analytes. Curr Appl Phys 20(11):1274–1280
39. Chen Z, Li H, Zhan S, He Z, Li B, Hui Xu (2015) Sensing characteristics based on Fano resonance in rectangular ring waveguide. Opt Commun 356:373–377
40. Wu T, Liu Y, Zhongyuan Yu, Ye H, Peng Y, Shu C, Yang C, Zhang W, He H (2015) A nanometeric temperature sensor based on plasmonic waveguide with an ethanol-sealed rectangular cavity. Opt Commun 339:1–6
41. Wang Q, Ouyang Z, Sun Y, Lin Mi, Liu Q (2019) Linearly tunable Fano resonance modes in a plasmonic nanostructure with a waveguide loaded with two rectangular cavities coupled by a circular cavity. Nanomaterials 9(5):678
42. Chen J, Li J, Liu X, Rohimah S, Tian H, Qi D (2021) Fano resonance in a MIM waveguide with double symmetric rectangular stubs and its sensing characteristics. Opt Commun 482:126563
43. Chen Y, Xu Y, Cao J (2019) Fano resonance sensing characteristics of MIM waveguide coupled square convex ring resonator with metallic baffle. Results Phys 14:102420
44. Su H, Yan S, Yang X, Guo J, Wang J, Hua E (2020) Sensing features of the Fano resonance in an MIM waveguide coupled with an elliptical ring resonant cavity. Nanomaterials 10(15):5096
45. El Haffar R, Farkhsi A, Mahboub O (2020) Optical properties of MIM plasmonic waveguide with an elliptical cavity resonator. Appl Phys A 126(7):1
46. He Z, Li C, Cui W, Xue W, Li Z, Pu L, Feng J, Xiao X, Wang X, Liu Y, Zou Q (2020) Dual-Fano resonances and sensing properties in the crossed ring-shaped metasurface. Results Phys 16:103140
47. Rahmatiyar M, Afsahi M, Danaie M (2020) Design of a refractive index plasmonic sensor based on a ring resonator coupled to a MIM waveguide containing tapered defects. Plasmonics 15:2169–2176
48. Liu H, Gao Y, Zhu B, Ren G, Jian S (2015) A T-shaped high resolution plasmonic demultiplexer based on perturbations of two nanoresonators. Opt Commun 334:164–169
49. Kamari M, Hayati M, Khosravi S (2021) Tunable infrared wide band-stop plasmonic filter using T-shaped resonators. Mater Sci Semicond Process 133:105983
50. Lu H, Liu X, Mao D, Wang L, Gong Y (2010) Tunable band-pass plasmonic waveguide filters with nanodisk resonators. Opt Express 18(17):17922–17927
51. Chao CT, Chau YF, Chiang HP (2021) Highly sensitive metal-insulator-metal plasmonic refractive index sensor with a centrally coupled nanoring containing defects. J Phys D Appl Phys 54(11):115301
52. Yan S, Zhang M, Zhao X, Zhang Y, Wang J, Jin W (2017) Refractive index sensor based on a metal–insulator–metal waveguide coupled with a symmetric structure. Sensors 17(12):2879
53. Chen W-C, Cardin A, Koirala M, Liu X, Tyler T, West KG, Bingham CM, Starr T, Starr AF, Jokerst NM, Padilla WJ (2016) Role of surface electromagnetic waves in metamaterial absorbers. Opt Express 24(6):6783–6792
54. Chau Y-F, Yeh H-H (2011) A comparative study of solid-silver and silver-shell nanodimers on surface plasmon resonances. J Nanopart Res 13:637–644
55. Chou Chau YF, Chen KH, Chiang HP, Lim CM, Huang HJ, Lai CH, Kumara NT (2019) Fabrication and characterization of a metallic–dielectric nanorod array by nanosphere lithography for plasmonic sensing application. Nanomaterials 9(12):1691
56. Sun YS, Chau YF, Yeh HH, Tsai DP (2018) Highly birefringent index-guiding photonic crystal fiber with squeezed differently sized air-holes in cladding. Jpn J Appl Phys 47(5R):3755
57. Johnson PB, Christy RW (1972) Optical constants of the noble metals. Phys Rev B 6(12):4370–4379
58. Moresco F, Rocca M, Zielasek V, Hildebrandt T, Henzler M (1997) Els-Leed study of the surface plasmon dispersion on Ag surfaces. Surf Sci 388(1):1–4
59. Wolff I, Knoppik N (1971) Microstrip ring resonator and dispersion measurement on microstrip lines. Electron Lett 7(26):779–781
60. Chen C, Sang-Hyun Oh, Li Mo (2020) Coupled-mode theory for plasmonic resonators integrated with silicon waveguides towards mid-infrared spectroscopic sensing. Opt Express 28(2):2020–2036
61. Lu H, Liu X, Mao D, Wang G (2012) Plasmonic nanosensor based on Fano resonance in waveguide-coupled resonators. Opt Lett 37(18):3780–3782
62. Yu J, Zhu J, Ye S, Wang X (2021) Ultra-wide sensing range plasmonic refractive index sensor based on a two-dimensional circular-hole grating engraved on a gold film. Results Phys 26:104396
63. Butt MA, Kaźmierczak A, Kazanskiy NL, Khonina SN (2021) Metal–insulator–metal waveguide-based racetrack integrated circular cavity for refractive index sensing application. Electronics 10(12):1419
64. Rakhshani MR (2019) Refractive index sensor based on concentric triple racetrack resonators side-coupled to metal–insulator–metal waveguide for glucose sensing. J Opt Soc Am B 36(10):2834–2842
65. Chau YF (2020) Mid-infrared sensing properties of a plasmonic metal–insulator–metal waveguide with a single stub including defects. J Phys D Appl Phys 53(11):115401
66. Chau YF, Chao CT, Huang HJ, Anwar U, Lim CM, Voo NY, Mahadi AH, Kumara NT, Chiang HP (2019) Plasmonic perfect absorber based on metal nanorod arrays connected with veins. Results Phys 15:102567
67. Chou Chau YF, Chou Chao CT, Huang HJ, Kooh MR, Kumara NT, Lim CM, Chiang HP (2020) Perfect dual-band absorber based on plasmonic effect with the cross-hair/nanorod combination. Nanomaterials 10(3):493

68. Chau YF, Jheng CY, Joe SF, Wang SF, Yang W, Jheng SC, Sun YS, Chu Y, Wei JH (2013) Structurally and materially sensitive hybrid surface plasmon modes in periodic silver-shell nanopearl and its dimer arrays. J Nanopart Res 15(3):1–3

69. Haffner C, Chelladurai D, Fedoryshyn Y, Josten A, Baeuerle B, Heni W, Watanabe T, Cui T, Cheng B, Saha S, Elder DL, Dalton LR, Boltasseva A, Shalaev VM, Kinsey N, Leuthold J (2018) Low-loss plasmon-assisted electro-optic modulator. Nature 556(7702):483–486

70. Ma Y, Li J, Han Z, Maeda H, Ma Y (2020) Bragg-mirror-assisted high-contrast plasmonic interferometers: concept and potential in terahertz sensing. Nanomaterials 10(7):1385

71. Pang S, Zhang Y, Huo Y, Xie Y, Hao L, Zhang T (2015) The filter characteristic research of metal–insulator–metal waveguide with double overlapping annular rings. Plasmonics 10(6):1723–1728

72. Wang Y, Li S, Zhang Y, Yu L (2016) Ultrasharp Fano resonances based on the circular cavity optimized by a metallic nanodisk. IEEE Photon J 8(6):1–8

73. Shi X, Ma L, Zhang Z, Tang Y, Zhang Y, Han J, Sun Y (2018) Dual Fano resonance control and refractive index sensors based on a plasmonic waveguide-coupled resonator system. Opt Commun 427:326–330

74. Vora A, Gwamuri J, Pala N, Kulkarni A, Pearce JM, Güney DÖ (2014) Exchanging ohmic losses in metamaterial absorbers with useful optical absorption for photovoltaics. Sci Rep 4(1):1–3

75. Rakhshani MR, Mansouri-Birjandi MA (2017) High sensitivity plasmonic refractive index sensing and its application for human blood group identification. Sens Actuators B Chem 249:168–76

76. Bijalwan A, Singh BK, Rastogi V (2021) Surface plasmon resonance-based sensors using nano-ribbons of graphene and WSe2. Plasmonics 15(4):1015–1023

77. Bijalwan A, Rastogi V (2017) Sensitivity enhancement of a conventional gold grating assisted surface plasmon resonance sensor by using a bimetallic configuration. Appl Opt 56(35):9606–9612

78. Eranti A, Kerola T, Aro AL, Tikkanen JT, Rissanen HA, Anttonen O, Junttila MJ, Knekt P, Huikuri HV (2016) Diabetes, glucose tolerance, and the risk of sudden cardiac death. BMC Cardiovasc Disorders 16(1):1–8

79. Mostufa S, Paul AK, Chakrabarti K (2021) Detection of hemoglobin in blood and urine glucose level samples using a graphene-coated SPR based biosensor. OSA Continuum 4(8):2164-2167

80. Sani MH, Khosroabadi S (2020) A novel design and analysis of high-sensitivity biosensor based on nano-cavity for detection of blood component, diabetes, cancer and glucose concentration. IEEE Sens J 20(13):7161–7168

81. Chau Y-F, Yang T-J, Lee W-D (2004) Coupling technique for efficient interfacing between silica waveguides and planar photonic crystal circuits. Appl Opt 43(36):6656–6663

82. Quazi SJ, Aslam N, Saleem H, Rahman J, Khan S (2020) Surgical margin of excision in basal cell carcinoma: a systematic review of literature. Cureus 12(7):e9211–e9311

83. Harhouz A, Hocini A (2021) Highly sensitive plasmonic temperature sensor based on fano resonances in MIM waveguide coupled with defective oval resonator. Opt Quant Electron 53(8):439

84. Zhu J, Lou J (2020) High-sensitivity Fano resonance temperature sensor in MIM waveguides coupled with a polydimethylsiloxane-sealed semi-square ring resonator. Results Phys 18:103183

85. Zhu J, Jin G (2021) Detecting the temperature of ethanol based on fano resonance spectra obtained using a metal-insulator-metal waveguide with Sio2 branches. Opt Mater Express 11(9):2787–2799

86. Wu T, Liu Y, Zhongyuan Yu, Ye H, Peng Y, Shu C, Yang C, Zhang W, He H (2015) A nanometeric temperature sensor based on plasmonic waveguide with an ethanol-sealed rectangular cavity. Opt Express 339:1–6

87. Liu X, Dan Wu, Chang Q, Zhou J, Zhang Y, Wang Z (2017) Grooved nanoplate assembly for rapid detection of surface enhanced Raman scattering. Nanoscale 9(40):15390–15396

88. Wu C, Ding H, Tianye Huang XuWu, Chen B, Ren K, Songnian Fu (2018) Plasmon-induced transparency and refractive index sensing in side-coupled stub-hexagon resonators. Plasmonics 13(1):251–257

89. Butt MA, Khonina SN, Kazanskiy NL (2019) Plasmonic refractive index sensor based on metal–insulator–metal waveguides with high sensitivity. J Mod Opt 66(9):1038–1043

90. Ding J, Qi Y, Yuan Y, Chen H, Liu W, Jia Y, Wang X (2021) Multiple fano resonances based on clockwork spring-shaped resonator for refractive index sensing. Phys Scr 96(12):125

Publisher's Note